JACS
JOURNAL OF THE AMERICAN CHEMICAL SOCIETY

Article

pubs.acs.org/JACS

Understanding the Roles of Anionic Redox and Oxygen Release during Electrochemical Cycling of Lithium-Rich Layered Li_4FeSbO_6

Eric McCalla,[†,‡,§,∥] Moulay Tahar Sougrati,[‡,§,⊥] Gwenaelle Rousse,[†,‡,§,#] Erik Jamstorp Berg,[▽] Artem Abakumov,[○] Nadir Recham,[◆] Kannadka Ramesha,[¶] Mariyappan Sathiya,[†,‡,§] Robert Dominko,[∥] Gustaaf Van Tendeloo,[⊥] Petr Novák,[▽] and Jean-Marie Tarascon*[,†,‡,§]

[†]Chimie du Solide et de l'Energie, FRE 3677, Collège de France, 11 place Marcelin Berthelot, 75231 Paris Cedex 05, France
[‡]ALISTORE-European Research Institute, FR CNRS 3104, 80039 Amiens, France
[§]Réseau sur le Stockage Electrochimique de l'Energie (RS2E), FR CNRS 3459, 80039 Amiens, France
[∥]National Institute of Chemistry, Hajdrihova 19, SI-1000 Ljubljana, Slovenia
[⊥]Institut Charles Gerhardt, CNRS UMR 5253, Université Montpellier 2, 34 095 Montpellier, France
[#]Sorbonne Universités - UPMC Univ Paris 06, 4 Place Jussieu, F-75005 Paris, France
[▽]Electrochemistry Laboratory, Paul Scherrer Institut, CH-5232 Villigen PSI, Switzerland
[○]EMAT, University of Antwerp, Groenenborgerlaan 171, B-2020, Antwerp, Belgium
[◆]LRCS, CNRS UMR 7314, Université de Picardie Jules Verne, 80039 Amiens, France
[¶]CSIR-CECRI Chennai unit, CSIR-Madras Complex, Taramani, Chennai 600 113, India

Supporting Information

ABSTRACT: Li-rich oxides continue to be of immense interest as potential next generation Li-ion battery positive electrodes, and yet the role of oxygen during cycling is still poorly understood. Here, the complex electrochemical behavior of Li_4FeSbO_6 materials is studied thoroughly with a variety of methods. Herein, we show that oxygen release occurs at a distinct voltage plateau from the peroxo/superoxo formation making this material ideal for revealing new aspects of oxygen redox processes in Li-rich oxides. Moreover, we directly demonstrate the limited reversibility of the oxygenated species (O_2^{n-}; n = 1, 2, 3) for the first time. We also find that during charge to 4.2 V iron is oxidized from +3 to an unusual +4 state with the concomitant formation of oxygenated species. Upon further charge to 5.0 V, an oxygen release process associated with the reduction of iron +4 to +3 is present, indicative of the reductive coupling mechanism between oxygen and metals previously reported. Thus, in full state of charge, lithium removal is fully compensated by oxygen only, as the iron and antimony are both very close to their pristine states. Besides, this charging step results in complex phase transformations that are ultimately destructive to the crystallinity of the material. Such findings again demonstrate the vital importance of fully understanding the behavior of oxygen in such systems. The consequences of these new aspects of the electrochemical behavior of lithium-rich oxides are discussed in detail.

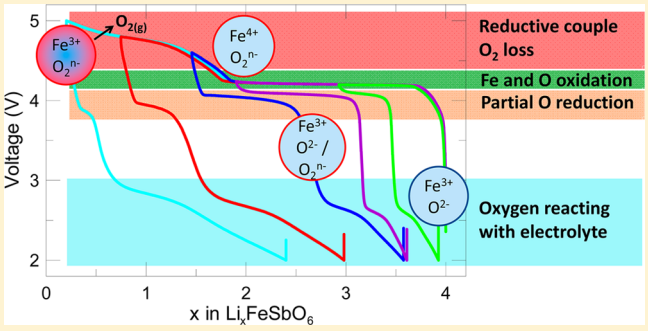

INTRODUCTION

In the ongoing search for new positive electrode materials with higher energy density, Li-rich layered oxides have emerged as one of the most promising classes of materials. In particular, Li-rich Ni−Mn−Co oxides (e.g., $Li_{1.2}Mn_{0.54}Co_{0.13}Ni_{0.13}O_2$), denoted hereafter NMC, show very high capacities but unfortunately also a high irreversible capacity and significant voltage fade with cycling.[1−3] Recently, Koga et al. demonstrated that although nickel and cobalt are oxidized during charging of the cells, a significant portion of the capacity comes from reversible oxygen redox in the material and not primarily due to oxygen gas release as previously reported in the literature.[1] Sathiya et al. further showed that in ruthenium containing materials, the oxygen oxidation results in peroxo/superoxo species[4,5] or, to be more general, oxygenated species of the form O_2^{n-} with n = 1, 2, or 3 (n = 2 represents the peroxo species, while n = 1 is the superoxo, n = 3 remains theoretical; we include it for completeness as it cannot be ruled out). This notation will be used here to represent oxygen in oxidation states above 2−, but not oxygen gas. Simply referring to O_2^{n-} therefore acknowledges that an unknown number of electrons are removed from any given oxygen and that there may

Received: February 9, 2015
Published: March 26, 2015

DOI: 10.1021/jacs.5b01424
J. Am. Chem. Soc. 2015, 137, 4804−4814

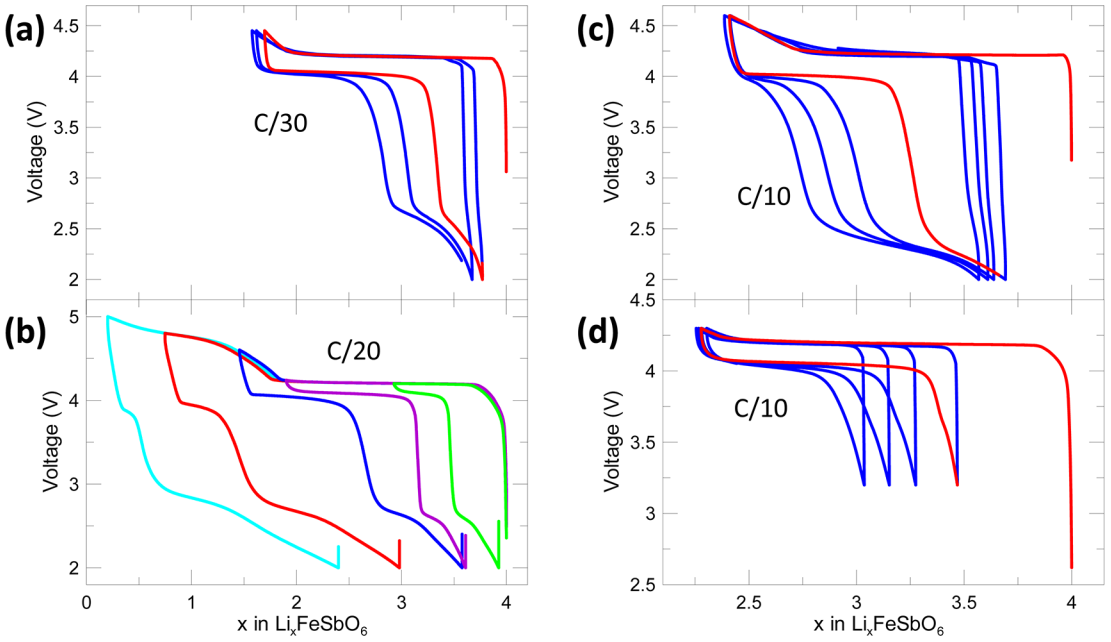

Figure 1. Galvanostatic cycling data for the Li_4FeSbO_6 sample. In panel (a) the cutoff voltages were 2 and 4.5 V, while for (c) they were 2 and 4.6 V and for (d) 3.2 and 4.3 V. In each of these, the first cycle is shown in red. In (b), only the first cycle is shown for samples with various cutoff conditions ($\Delta x = 1$ in green, others have voltage cutoffs of 4.25, 4.6, 4.8, and 5.0 V).

in fact be a distribution of the three *n* values. In the case of oxygen gas being released from the material the result will be oxygen vacancies. Thus, in this article, oxygenated species will be used to refer to oxygen that has been oxidized beyond 2− and is still within the material, while oxygen vacancies will refer to oxygen being released irreversibly from the material.

In both the NMC and ruthenium-based systems where reversible oxygen redox has been studied, there remains an important ambiguity related to oxidation states during discharge. In NMC materials, it is often reported that some manganese is reduced from its pristine oxidation state of 4+ to 3+, and this increases with cycling with accompanied structural changes toward a spinel-like material.[6,7] In contrast, a recent study on one particular NMC composition suggests changes in manganese oxidation are quite limited.[8] In Li−Ru−Ti−O materials, it is clear that a significant amount of titanium is reduced to 3+ during discharge.[5] In both of these cases, the reduction of transition metals to states lower than those found in the pristine material during discharge implies that not all oxidation processes taking place during charge are completely reversed during discharge. This has typically been attributed to irreversible oxygen vacancy formation. It has never been possible to directly observe if the oxygenated species formation is completely reversible because both processes (oxygenated species and oxygen vacancy formations) occur at similar potentials. However, here, it will be demonstrated that oxygen vacancies form at a higher voltage in Li−Fe−Sb−O than the oxygenated species such that there is finally an opportunity to directly probe the reversibility of the oxygenated species.

Another significant subject from the literature comes from Li-air battery research performed using carbonate-based electrolytes. The desired mechanism for a Li-air cell during discharge involves oxygen gas being oxidized to form a superoxo radical which then reacts with lithium. However, this second step does not occur in carbonate-based electrolytes. Instead the superoxo radical, $O_2^{1-\bullet}$, is reduced while reacting with the alkyl carbonates in the electrolyte to form a variety of products including Li_2CO_3, $C_3H_6(OCO_2Li)_2$ and CH_3CO_2Li at a potential of approximately 2.6 V vs Li/Li^+.[9−11] During the next charge, these products oxidize and give off carbon dioxide and water. With continued cycling, films form on both the positive and negative electrodes which contribute to capacity fade and eventual cell failure. This same behavior is seen here for Li−Fe−Sb−O samples discharged below 3.0 V, so the work performed in Li-air research will be of significance. This same mechanism was proposed to occur in Li-rich NMC cells after oxygen gas is produced during first charge by Yabuuchi et al.,[12] but no gas emission measurements were made to confirm this. Yabuuchi et al. also did not consider the possibility of superoxo in the particles, as this mechanism was not yet proposed in the literature.

Recently, we have presented the structure of pristine materials with compositions near that of Li_4FeSbO_6.[13] It was found that the materials commonly referred to as Li_4FeSbO_6 (ref 14) were in fact slighly lithium deficient such that metal site vacancies exist in the material, as previously seen in some Li−Ni−Mn−O materials.[15] Here, the material studied has approximately 3.5 lithium per formula unit, it is the sample labeled B0* in ref 13. This material is selected for further study here as it showed the best electrochemical performance, but all of the Li−Fe−Sb−O voltage curves had the same features, and the conclusions drawn here can easily be applied to all the electrochemical data in ref 13. The structure is typical for lithium-rich oxides: alternating layers labeled "lithium" and "transition-metal" layers, where Li, Fe, and Sb all order on the transition-metal layer, while the lithium layer is filled solely with lithium. The oxygen close packed layers are stacked in an O3 pattern. To date, electrochemical data on this material have been extremely limited as it has primarily been studied for its magnetic properties.[14] Furthermore, although a wide variety of experimental methods are used in this study, it should be noted that due to overlap between antimony and oxygen transitions, XPS data cannot be used here to identify the presence of O_2^{n-} species, as previously used in refs 4 and 5. Instead, we indirectly observe the presence of peroxo species by combining SQUID data with both Fe and Sb Mössbauer data as

DOI: 10.1021/jacs.5b01424
J. Am. Chem. Soc. 2015, 137, 4804−4814

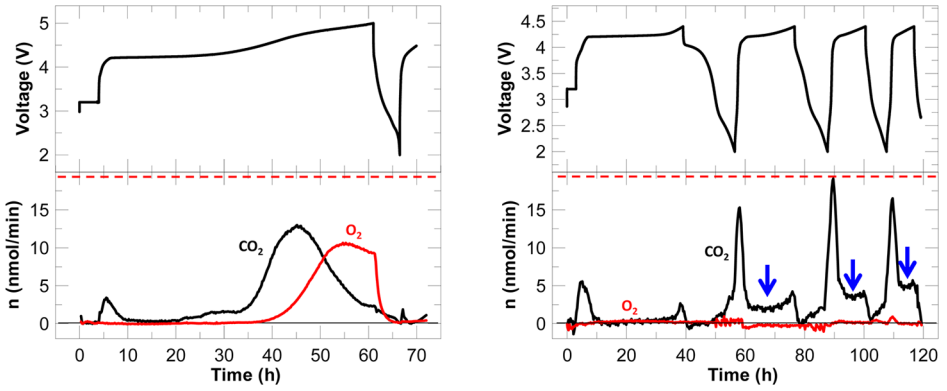

Figure 2. DEMS data showing the oxygen and carbon dioxide released during cycling with two different cutoff voltages: 5.0 V (left) and 4.4 V (right). The red dashed lines represent the amount of oxygen that would be released if the current was entirely due to O^{2-} converting to O_2 gas. The blue arrows indicate regions of carbon dioxide production during charging beyond the first cycle, referred to in the text.

will be described in the Results section. All details of the experimental methods used are included in Supporting Information.

RESULTS

Summary of Electrochemical Data. Figure 1 shows electrochemical cycling data for cells made from Li_4FeSbO_6 material cycled under various conditions. As discussed in ref 13, the pristine material has composition $Li_{3.54}FeSb_{1.1}O_6$. As such, it is slightly lithium deficient, but for simplicity, all cycling data presented here are expressed with a starting point of $x = 4$ and not 3.54. Figure 1a shows a large plateau at 4.2 V which is partially reversed upon discharge. It is tempting to view the part of the charge above the 4.2 V plateau as simply being the onset of electrolyte oxidation; however Figure 1b shows that there is a large capacity at voltages above 4.3 V, and this is not typical for electrolyte decomposition. Furthermore, the discharge curves change drastically when charged above 4.3 V, with a drop in the discharge voltage of the plateau near 4.0 V and a large reduction in the capacity on this plateau when charged above 4.5 V. Figure 1a shows that at C/30, the first charge up to 4.5 V involves the transfer of 2.3 Li per formula unit or roughly 205 mAh/g. However, discharge down to 3.0 V is only about 1.7 Li or 151 mAh/g, with the primary reduction taking place at about 4.0 V. This plateau fades rapidly with cycling, with the third discharge being approximately half of that obtained on the first cycle, and this corresponds with an increase in the capacity below 3.0 V, constituting a very extreme case of voltage fade as cycling progresses here, and this low voltage capacity is not of value for positive electrode materials. The cells cycled at C/10 (Figure 1c,d) show reduced capacity (first charge of 1.6 Li only) showing poor rate performance typical for lithium-rich oxides. The decrease in the discharge plateau at 4.0 V is also very rapid when cycled with down to 2.0 V at C/10, and this effect is much slower when the cutoff discharge voltage is 3.0 V. Nonetheless, regardless of the conditions used, there is always irreversible capacity on every cycle down to 3.0 V, or put differently, at every cycle the 4 V discharge plateau diminishes. Figure S.1 shows that this same behavior is obtained even if cycling is limited by charge capacity ($\Delta x = 0.5$ and 1.0 are shown). Therefore, no conditions were found under which the discharge plateau near 4.0 V remains stable with cycling.

Figure 2 shows the differential electrochemical mass spectrometry (DEMS) results for Li_4FeSbO_6 materials cycled to either 4.4 or 4.6 V. Both sets of data show that a negligible amount of oxygen is released during the charge plateau at 4.2 V, especially in comparison to the red dashed line representing the amount of oxygen that would need to be released to account for the current measured in the cell. By contrast, there is significant oxygen release taking place above 4.5 V, though this is still insufficient to account for the total current. As will be demonstrated in the next section, peroxo species form during the plateau at 4.2 V such that this is an opportunity to study this process free of oxygen release which occurs simultaneously in Li-rich NMC materials. Also, since iron and antimony are not reduced below their pristine states of 3+ and 5+, respectively, in the voltage ranges studied here (as will be clearly demonstrated from Mössbauer data below), this study represents the first opportunity to observe the reversibility of the peroxo species without the extra signals from reduction of the metals, such as manganese in NMC.

Each plateau of the electrochemical curve involves very different mechanisms and result in significant structural changes. Thus, the rest of the Results section is organized according to features in the electrochemical voltage curve.

Charge Plateau at 4.2 V. Figure S.2 shows SQUID data for each of the pristine, charged to 4.6 V and discharged to 3.0 V samples. As described in Supporting Information, the data were corrected for carbon with the use of $_o$ in the equation for magnetic susceptibility: $\chi = \chi_o + C/(T - \theta)$ where C is used to calculate the effective moment, θ is the Curie temperature, and χ_o is a diamagnetic contribution from carbon black and any biproducts of reactions with the electrolyte. The fits are shown in Figure S.2. The fact that these graphs of $1/(\chi\text{-}\chi_o)$ vs T are perfectly linear shows the effectiveness of using χ_o. Table 1 shows that the effective moments, μ_{eff}, confirm that the iron is in the 3+ oxidation state for both the pristine and the sample discharged to 3.0 V with excellent agreement between the experimental values of 5.89 μ_B and 5.96 μ_B and the theoretical value of 5.92 μ_B. By contrast, the effective moment for the sample charged to 4.6 V shows that iron is in the low spin 4+ state, again with a good agreement with the theoretical value (2.71 versus 2.82 μ_B). Of particular importance to the discussion to follow, the effective moment of the charged sample, 2.71 μ_B, is not at all consistent with that of Fe^{5+} (3.87 μ_B). Thus, the oxidation state of iron in the sample charged to beyond the 4.2 V plateau is 4+.

Figure 3 shows combined in situ XRD and ^{57}Fe Mössbauer data for a sample charged to 4.5 V at C/40 and discharged to 3.0 V. The change in the XRD peaks is indicative of a two-phase transition (shown over a wider scattering angle range in Figure

DOI: 10.1021/jacs.5b01424
J. Am. Chem. Soc. 2015, 137, 4804−4814

Table 1. Values for Effective Magnetic Moment[a]

sample	μ_{eff}/μ_B
Experimental	
pristine	5.96(3)
charged 4.6 V	2.71(2)
discharged 3.0 V	5.89(3)
Theoretical	
Fe^{3+} HS	5.92
Fe^{4+} LS	2.82
Fe^{4+} HS	4.89
Fe^{5+} LS	3.87

[a]Experimental results obtained fitting data over range of 50−350 K as shown in Figure S.2. Theoretical values were obtained with the spin only formula: $2\sqrt{(S(S+1))}$.

S.3). The structure of the sample in the charged state will be discussed below. The XRD pattern of the material discharged to 3.0 V matches that of the pristine, though with broadened peaks, suggesting crystallites have shrunk during cycling, perhaps via fracturing. Figure 4 shows ex situ XRD patterns at key stages during cycling, and after chemical delithiation. The pattern after charging to 4.7 V confirms the changes seen in the in situ data, and the sample that was then discharged to 2.0 V again shows the same pattern as the pristine. The ^{57}Fe Mössbauer data, Figures 3 and 5, show that the Fe^{3+} in the pristine material is converted to an oxidized Fe, labeled Fe^{4+} based on the SQUID data. Upon discharge, the oxidized iron is converted back to Fe^{3+}, a process which is completed at 3.0 V after the reinsertion of about 1.5 Li.

Table 2 and Figure S.4 shows the fitted parameters obtained from the ^{57}Fe Mössbauer data. The value of the isomer shift for the Fe^{3+} species is consistent with that observed in the literature for this species in an octahedral oxygen environment.[16] However, the isomer shift of −0.37 mm/s is low for Fe^{4+}. The lowest value for Fe^{4+} in octahedral oxgyen is −0.20 mm/s, and the only values for Fe^{5+} in such an environment are −0.57 and −0.40 mm/s.[17,18] Both the SQUID results and the fact that only 1.5 Li is required during discharge to completely reduce the iron back to 3+ demonstrate that iron is best described as being in the low spin 4+ oxidation state. An isomer shift of −0.25 mm/s is reported for

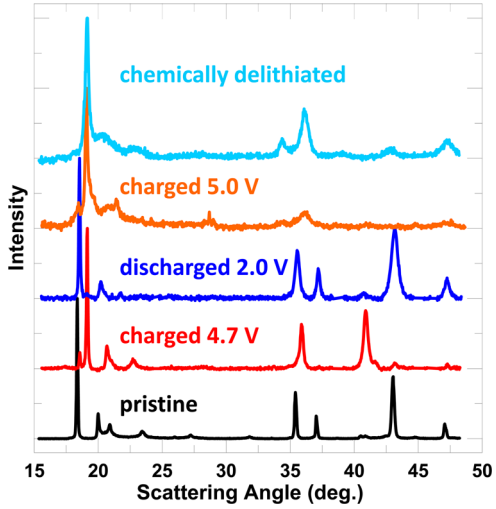

Figure 4. Cu Kα XRD spectra of Li_4FeSbO_6 at various states of charge. The discharged 2.0 V sample was first charged to 4.7 V.

Fe^{4+} in the charged state in Li_3FeN_2, and the authors attribute the low isomer shift (they expected a shift of 0.0 mm/s for a tetrahedral N environment) to Fe^{4+} being in the low spin state.[19] Here, SQUID showed that Fe^{4+} is in the low spin state such that some of the low isomer spin can be attributed to this effect, but it is still likely that the iron is in an unusual environment reducing the value further to −0.35 mm/s. The two possible mechanisms that can give both a capacity of at least 1 lithium per formula unit and reduce the Fe isomer shift significantly are the formations of oxygen deficiencies (reducing the coordination reduces the isomer shift)[16] and/or the formation of O_2^{n-} (the isomer shift decreases when a nearby atom is oxidized as seen with Sb below). Electrolyte oxidation is dismissed here as it would occur only at the surface and so would not systematically change the iron environment in the bulk of the particles. Furthermore, as shown in Figure 2, the oxygen release during the plateau at 4.2 V is negligible and certainly cannot account for the systematic decrease in isomer shift of the Fe^{4+} species (also, as shown below, only 0.11 lithium needs to be removed to saturate the electrolyte

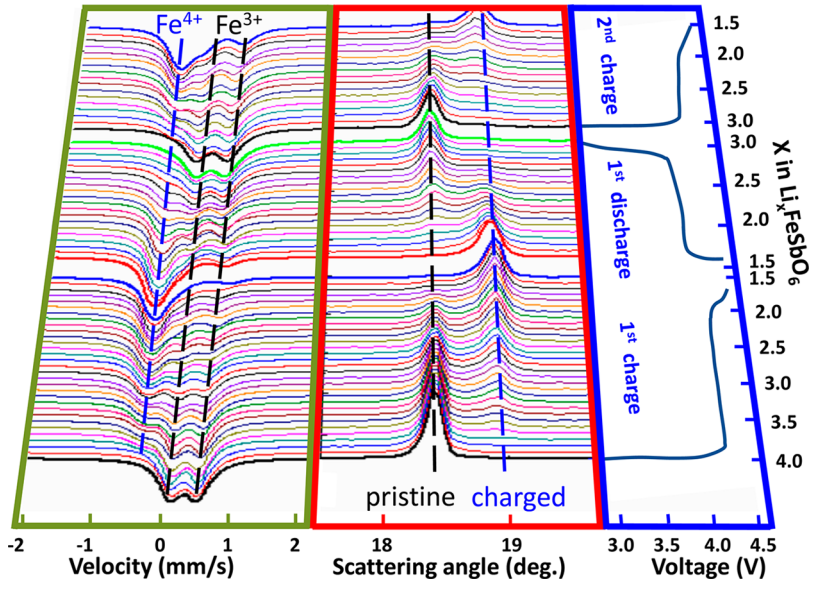

Figure 3. In situ XRD and Mössbauer data obtained for a Li_4FeSbO_6 cycled at C/40.

DOI: 10.1021/jacs.5b01424
J. Am. Chem. Soc. 2015, 137, 4804−4814

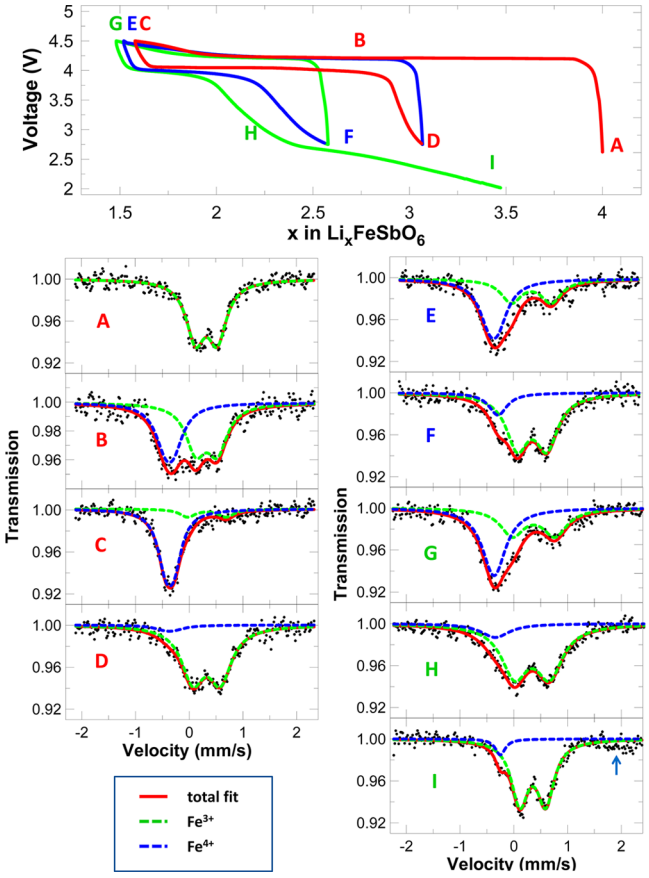

Figure 5. A selection of key ^{57}Fe Mössbauer spectra from the in situ cell, along with the fits obtained with two sites: Fe^{3+} and Fe^{4+}. The blue arrow indicates trace Fe^{2+} appearing during deep discharge. In the voltage curve, the first cycle is shown in red, the second in blue, and the third in green, the letters indicating each scan use the same color scheme. It should be noted that the small amount of Fe4+ in the discharged state (D) here is on the order of the noise in the background and is therefore considered to be negligible, consistent with SQUID results showing only Fe^{3+} at 3.0 V.

such that dissolved oxygen undetected by DEMS does not account for the extra lithium extracted at 4.2 V). As such, the only mechanism that accounts for the extra capacity on charge, and the systematic decrease in isomer shift is the formation of oxygenated species. This will also be shown to be consistent with ^{121}Sb Mössbauer data below. Although we acknowledge that we are using simple representations to explain very complex electronic structures, the best description of the redox process occurring on the 4.2 V plateau is that iron is oxidized to Fe^{4+} with some of the neighboring oxygens being oxidized above 2-. The formation of peroxo-like species at a potential of 4.2 V is not new for Li-rich oxides as this is the potential found in ruthenium containing compounds,[4,5,20,21] but this is the first case where a two-electron process is observed which results in O_2^{n-} (i.e., the oxidation of the metal and oxygen occur simultaneously here). The simultaneous presence of Fe^{4+} and a peroxo species therefore results in an electron density (in particular the nonvalence electrons) quite similar to that of Fe^{5+} explaining the low isomer shift, while the valence electrons affecting magnetic properties would be that of Fe^{4+}.

Figure S.5 shows the ^{121}Sb Mössbauer data for each of the pristine charged to 4.6 V and discharged to either 3.0 or 2.0 V. Table 3 shows the corresponding fitted parameters. The isomer shift versus $CaSnO_3$ expected for Sb^{5+} is about 0.2 mm/s, while that of Sb^{3+} is roughly −15 mm/s (ref 22). Clearly, the oxidation state of antimony is not changing, but the isomer shift is affected by oxidized species nearby which results in a shift to lower values. In the charged sample, the isomer shift is displaced by −0.4 mm/s (no where near the change that is expected if Sb changes oxidation state, but this is consistent with a shift due the presence of oxidized species nearby). We therefore attribute this shift to the presence of Fe^{4+} and O_2^{n-}. At 3 V, 97.4% of all Fe is in the 3+ state as shown in Table 2, but the Sb isomer shift is still 0.2 mm/s lower than in the pristine. This shows there is still some oxidized species nearby, as expected if some of the oxygenated

Table 3. ^{121}Sb Mössbauer Parameter Results for Samples Measured at 10 K, Determined Based on the Fits in Figure S.5

sample	isomer shift (mm/s)	line width (mm/s)
pristine	0.17 (1)	4.31(3)
charge 4.6 V	−0.24(1)	3.28(4)
discharge 3.0 V	−0.03(1)	3.62(3)
discharge 2.0 V	0.08(1)	3.37(3)

Table 2. Fitted Values for Isomer Shift, Quadrupole Splitting, Line Width and Contributions Obtained by Iron Mössbauer Spectroscopy[a]

sample	components	IS (mm/s)	QS (mm/s)	LW (mm/s)	contribution (±3%)
pristine	Fe^{3+}	0.33(1)	0.39(2)	0.32(3)	100
charged 4.5 V[b]	Fe^{4+}	−0.36(1)	0.16(4)	0.36(5)	85.5
	Fe^{3+}	0.33(7)	0.72(10)	0.36(5)	14.5
discharged 3.0 V[b]	Fe^{4+}	−0.37[c]	0.16[c]	0.54(5)	2.6
	Fe^{3+}	0.31(2)	0.54(2)	0.54(5)	97.4
charged 4.5 V cycle 2[b]	Fe^{4+}	−0.37[c]	0.16[c]	0.47(5)	59.6
	Fe^{3+}	0.33(7)	0.74(5)	0.47(5)	40.4
chemically delithiated	Fe^{3+} (site A)	0.35(2)	0.65(3)	0.42(2)	47
	Fe^{3+} (site B)	0.35(2)	0.97(3)	0.42(2)	53
	Fe^{4+}	−0.37(5)	0.21(5)	0.32(5)	14
charged 5.0 V	Fe^{3+} (site A)	0.35(2)	0.75(3)	0.47(2)	61
	Fe^{3+} (site B)	0.32(4)	1.34(10)	0.47(3)	25

[a]Complete graphs with the parameters during cycling of the in situ cell are included in Figure S.4. Isomer shifts are given relative to a Fe standard at room temperature. [b]These measurements were obtained in the in situ cell (data in Figure 3). Here line widths of Fe^{4+} and Fe^{3+} were constrained to be equal. [c]Parameters constrained during fit.

DOI: 10.1021/jacs.5b01424
J. Am. Chem. Soc. 2015, 137, 4804−4814

species are not reversible. By contrast, at 2 V the value has increased back closer to that of the pristine material. This displacement of the antimony isomer shift is therefore consistent with the conclusion that O_2^{n-} is present both at 4.2 V and partially at 3.0 V at which point all iron has returned to the pristine 3+ state. This lends support to the above argument that iron is in fact in the 4+ state in an unusual environment due to the oxygenated species nearby.

Figure 4 also clearly shows the dramatic changes in the XRD patterns at various states of charge. The pattern for the sample charged at 4.7 V is very different from the pristine and it matched that seen in the in situ to 4.5 V as well as a sample charged to 4.3 V in Figure 6. These patterns cannot be indexed in $R\bar{3}m$, even if we

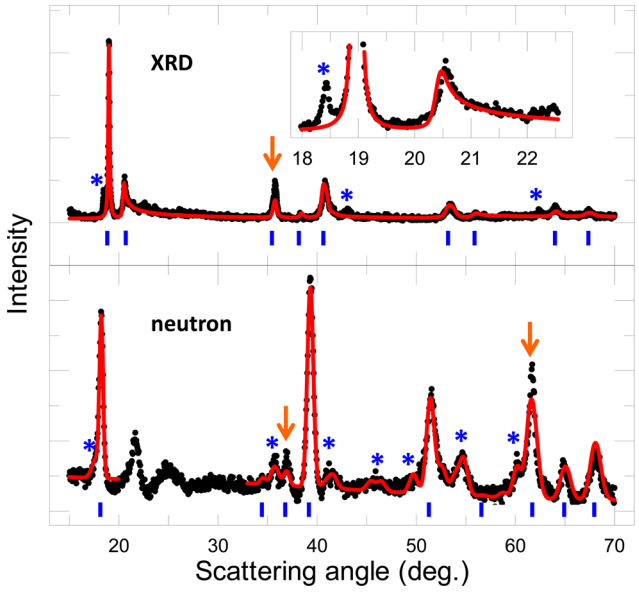

Figure 6. Fits of XRD (Cu Kα) and neutron (λ = 1.494 Å) scattering measured for a sample charged to 4.3 V. The * marks peaks from the pristine material. The pristine phase was not included in the fit for the XRD pattern which was performed using FAULTS. The pristine phase was necessary to obtain a quality fit to the neutron data because the broader peaks resulted in overlap between peaks from the pristine and charged phases. Le Bail refinement was used to describe the pristine phase. The orange arrows mark the peaks where the experimental intensity is significantly larger than that obtained for the refinement, as discussed in text.

ignore the superstructure peaks, implying than an O3 stacking is no longer present. Instead, it can be indexed in $P\bar{3}m1$ space group (once again ignoring the superstructure peaks), which takes an O1 stacking of the oxygen octahedra, as shown in Figure 7. By contrast to these three charged samples (4.3, 4.5, and 4.7 V) the samples charged to 5.0 V or chemically delithiated (equivalent potential of 5.1 V, ref 1) show very different XRD patterns and will be considered in the next section dealing with capacity above 4.3 V.

The structure of the material charged to the end of the 4.2 V plateau was determined using XRD, neutron scattering and HRTEM measurements. Figure 6 show the XRD and neutron patterns for a sample charged to 4.3 V (the 1.5 g of this sample were prepared in a large cell as described in Supporting Information). Both scans can be indexed in the $P\bar{3}m1$ space group with the transition metals at (0, 0, 0), oxygen atoms at (1/3, 2/3, z_o), and the partially occupied lithium layer at (0, 0, 1/2). After subtracting the signal for carbon from the neutron data,

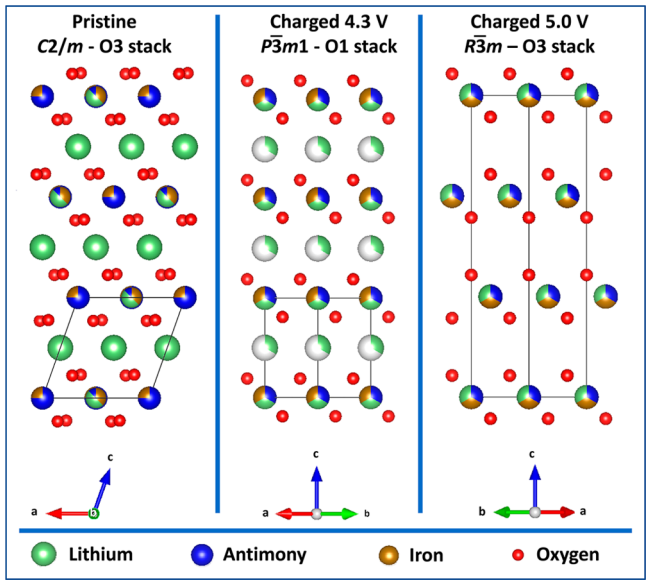

Figure 7. Primary structures throughout first charge. No efforts are made in these diagrams to correctly show the ordering on the transition-metal layers, though this ordering is present to varying degrees throughout. The structure shown for 5.0 V is the predominate structure established from XRD and neutron scattering, and the minority phase is included in Figure S.10.

as described in the Supporting Information, a good fit is obtained with this $P\bar{3}m1$ representation, as shown in Figure 6, with only intensity differences at two peaks marked with arrows. This fit yields a = 2.9088(6) Å, c = 4.722(2) Å, z_o = 0.199, n_o = 1 (occupation of the oxygen site). Also, the transition-metal layer has composition $Sb_{1.1}FeLi$, and there is 1 lithium on lithium layer, matching the overall composition of $Li_2FeSb_{1.1}O_6$ expected from the fact that 1.5 lithiums were removed from the pristine $Li_{3.54}FeSb_{1.1}O_6$ material. There are a number of challenges with respect to fitting neutron data of charged samples which deserve some attention. First, the correction for the presence of carbon is difficult and resulted in this case in a very strange background beyond 70° thereby limiting the angle range of value for fitting (Figure S.6). Furthermore, the presence of a small amount of pristine material had to be taken into account as there were overlapping peaks (not the case for the sharper peaks in the XRD patterns). As a result, no further efforts were made to refine the neutron data.

In contrast to the neutron data, the XRD pattern of the sample charged to 4.3 V could be refined as a single phase (the pristine peaks, marked with * in Figure 6, did not overlap with the peaks from the charged phase). As such, the program FAULTS was used to refine the XRD pattern while taking stacking faults into account. The procedure followed is described in detail in ref 13 with the variation here that the x coordinates of the stacking vectors, $\mathbf{S}_{1x}$ and $\mathbf{S}_{2x}$, are both 0 in order to give O1 stacking. The composition of each layer was identical to that used to refine the neutron data, with the extra constraint that the transition-metal layer was fully ordered, the coordinates used are given in ref 13. The XRD fit in Figure 6 was obtained assuming random stacking of the layers and shows a very good agreement with the data for the first superstructure peak at 20.7°. For comparison purposes, the lattice parameters (though this is not strictly a unit cell anymore with stacking faults taken into account) obtained with FAULTS are a = 5.035(1) Å (or a = 2.907(1) Å expressed in the $P\bar{3}m1$ geometry), b = 8.713(2) Å (or a = 2.904(1) Å in $P\bar{3}m1$), c

DOI: 10.1021/jacs.5b01424
J. Am. Chem. Soc. 2015, 137, 4804−4814

= 4.692(1) Å, and z_o = 0.24(1). All these parameters match up relatively well with that obtained from the neutron data, and the fit overall is excellent; except for the peak near 36° where the experimental peak is double that of the one for the fit. This mismatch also occurred when fit with the $P\bar{3}m1$ space group. It is unclear as to the cause of the extra intensity on this one peak, but it is clear that the O1 structure shown in Figure 7 is a good description of the material after charging to 4.3 V (and even 4.7 V, where the XRD pattern shows little difference). Again, the O1 stacking here refers to the oxygen octahedra only given that the transition-metal layers are ordered.

To study the local structure more closely, TEM investigation was performed on a sample charged to 4.6 V (the XRD pattern matches that of the sample charged to 4.3 V, but DEMS does show that some oxygen release has occurred by this point). Figure S.7 shows electron diffraction patterns of this sample with the outlined reciprocal unit cell corresponding to the hexagonal O1 $P\bar{3}m1$ structure with $a \approx 2.9$ Å, $c \approx 4.7$ Å. In the [001] ED pattern, this unit cell corresponds to the brightest spots. Besides these spots, weaker spots are seen at the 1/3[110] and 2/3[110] reciprocal lattice positions. These spots are tentatively ascribed to the cation ordering. The [100] and [1$\bar{2}$0] ED patterns reveal absence of the regular reflections which could be undoubtedly attributed to a certain sequence of the close packed layers (except of the 00l reflections, common for all sequences). Instead, diffuse intensity lines are present. In the [1$\bar{2}$0] ED pattern, which allows differentiating the O1 and O3 structures, the diffuse lines are modulated with the intensity maxima roughly at the positions which are characteristic for the O1 structure with the "hexagonal" ABAB close packing. In the [100] ED pattern, which is sensitive to the cation ordering, the extra diffuse intensity lines 1/3 1/3 l and 2/3 2/3 l are visible. Their intersection with the Ewald sphere causes extra spots in the [001] ED pattern. These diffuse lines can originate from stacking faults in the "honeycomb" cation ordering at the octahedral interstices between the close packed oxygen layers.

The [1-20] and [100] HAADF-STEM images of the sample charged to 4.6 V, illustrating stacking faults in both the sequence of the close packed oxygen layers and the "honeycomb" cation ordering, are shown in Figure 8. The material consists of a mixture of domains with the "hexagonal" ABAB (O1) and "cubic" ABCABC (O3) close packed sequences, where stacking faults are also present. The "honeycomb" cation ordering corresponds to the M−Li−Li−M−Li−Li−M scheme, where "M" can be both Fe and Sb and "Li" can contain vacancies. The sequence of the "honeycomb" layers along the c-axis is very disordered because the layers can be laterally displaced with respect to each other by 0, ±1/3 of the M − M separation. The TEM results are therefore consistent with the XRD results showing primarily O1 stacking with ordered sublattices which have a high amount of stacking faults.

Charge Capacity Above 4.3 V. Figure 1b shows the cycling curve when a sample is charged to 5.0 V. Clearly there is a large amount of capacity beyond the 4.2 V plateau, and this results in a dramatic change in the subsequent discharge curve. In particular, the highly oxidized sample shows a large decrease in the length of the 4 V plateau, and the voltage of this plateau decreases dramatically as well. The XRD pattern of the sample charged to 5.0 V in Figure 4 shows that the material is still crystalline, but peaks are far broader than in any other sample; the pattern is also very different from that obtained after charging to lower voltages (even 4.7 V). Due to the poor crystallinity of this sample, it proved useful to study the chemically oxidized sample obtained

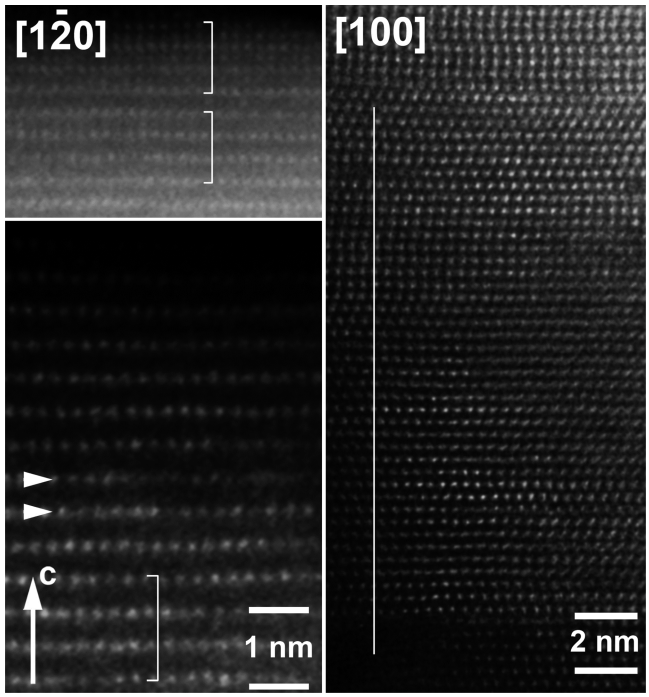

Figure 8. [1$\bar{2}$0] and [100] HAADF-STEM images of the sample charged to 4.6 V. The blocks of the "hexagonal" ABAB close packing are marked with square brackets in the [1$\bar{2}$0] image. The arrowheads mark single stacking faults in the "cubic" ABCABC close packed domains. The pattern of the bright dots in the [100] image corresponds to the M−Li−Li−M−Li−Li−M ordered sequence along the layers (M can be both Fe and Sb, and Li can contain vacancies). A vertical line is a guide to the eye to monitor the lateral displacements of the layers by ±1/3 of the M − M separation.

using NO_2BF_4 as described in the Supporting Information (the redox couple operates at about 5.1 V).[1] Table 4 shows the

Table 4. Values for Metallic Composition Obtained with ICP[a]

sample	Fe (±0.05)	Li	Sb (±0.06)
pristine	1.00	3.54(18)	1.10
delithiated 1 d	0.90	1.10(6)	1.21
delithiated 3 d	0.90	0.73(4)	1.21
delithiated 7 d	0.96	0.83(4)	1.14
relithiated	0.95	1.02(5)	1.15
charged 4.8 V	1.04	0.94(5)	1.06
discharged 2.0 V	1.03	3.18(16)	1.07

[a]All values are normalized such that the oxygen content of the pristine is 1 (assuming Fe^{3+} and Sb^{5+}), and all other samples have the same value for Fe + Sb as the pristine sample. The relithiated sample is obtained by reacting LiI with the sample obtained after 3 days of chemical delithiation.

elemental analysis for the chemically oxidized materials as well as a sample charged to 4.8 V. The values show that electrochemical and chemical delithiation give roughly the same compositions, though chemical delithiation may also dissolve a small amount of iron from the samples. Also, relithiation with LiI (approximately 3.0 V potential, ref 1) results in only 0.2 or 0.3 lithium reinsertion. Figure 4 shows that the XRD pattern from a sample that was chemically delithiated for 48 h matches that of the sample charged to 5.0 V, with the pair of peaks near 35° having the same intensity ratio. However, charging to 5.0 V is far more destructive with broader XRD peaks which suggest very small and strained

DOI: 10.1021/jacs.5b01424
J. Am. Chem. Soc. 2015, 137, 4804−4814

crystallites and/or multiple phases with overlapping peaks. Figure S.8 shows the cycling data for the chemically delithiated sample. This discharge curve has no capacity above 3.3 V, very little down to 3.0 V (consistent with chemical relithiation), and allows for about 0.8 Li to be reinserted down to 2.0 V, which matches closely with that obtained for the fourth cycle up to 4.5 V in Figure 1c. In contrast, the sample charged to 5.0 V in Figure 1 shows a minor plateau near 4.0 V and then a greater capacity below 3.0 V. The features of this curve, below 3.0 V, will be discussed in the next section. It is sufficient now to show that both the XRD matches that of the sample charged up to 5.0 V.

Of particular interest to the lithium-ion battery community should be the results of the Mössbauer spectroscopy of these highly oxidized materials. Figure 9 shows the Fe spectra for both

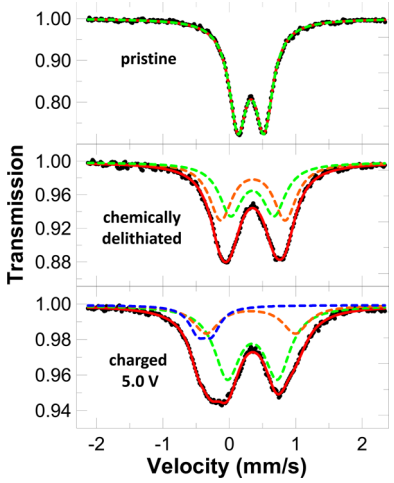

Figure 9. Iron Mössbauer data of highly charged samples, along with fits which include one Fe^{4+} site in blue, and two Fe^{3+} sites in orange and green.

the chemically delithiated and charged to 5.0 V samples. Table 3 shows the resulting parameter values. The chemically delithiated sample is entirely made up of Fe in the 3+ state, though more than one site is required to accurately describe the data. The sample charged to 5.0 V shows that most Fe has been reduced to 3+, again with at least two different environments, both heavily distorted indicated by the large quadrupole splits. There is also a small amount of Fe^{4+} remaining at 5.0 V, which suggests that the equilibrium state reached during chemically delithiation has not been attained. Nonetheless, it is clear that upon further oxidation beyond the 2 lithium removed up to 4.3 V, there is further oxidation of oxygen with a reductive coupling with the iron resulting in the vast majority of iron returning to the initial oxidation state of 3+. Both sites have very large quadrupole splitting indicative of very distorted environments, consistent with our findings that much oxygenated species exist in this sample (i.e., current resulting from oxygen loss in Figure 2 is far too small to account for the total first charge capacity). Also, the presence of two environments can be attributed to the surface being modified as discussed further below.

Due to its better crystallinity, the chemically delithiated sample was studied to determine the structure of the highly oxidized samples. The XRD and neutron patterns both indexed nicely in the $R\bar{3}m$ space group (i.e., O3 stacking). Figure S.9 shows single phase refinements for both XRD and neutron scattering for this material. The structure used had the transition-metal layer atoms at (0, 0, 0) and O at (0, 0, z_{ox}) with the occupation of oxygen being n_o. The Li layer was therefore left empty (though this condition was lifted to try and improve the neutron fit and this failed). The composition of the transition-metal layer was based on the ICP data in Table 4. Although both the neutron and XRD peaks indexed well with the $R\bar{3}m$ space group, the model gave a very poor fit to the neutron scattering data. Furthermore, the inset shows that although the superstructure peaks in the XRD patterns are at the correct positions, the experimental intensities are much larger than in the calculated pattern (again, FAULTS was used here to account for stacking faults).

In order to fit both the XRD and neutron data accurately, two phases were required. This approach is based on recent reports for Li-rich NMC materials at the top of charge, where two phases are found with one being oxygen deficient and present at the surface of particles.[23,24] Given that there is little data here to constrain two phases, a simple model was used: both phases were expressed in the $R\bar{3}m$ space group with the same metal compositions: $Li_{0.8}FeSb_{1.1}O_{6-\delta}$ (i.e., the composition after 1 week of delithiation). Figure 10 and Table 5 show the results of

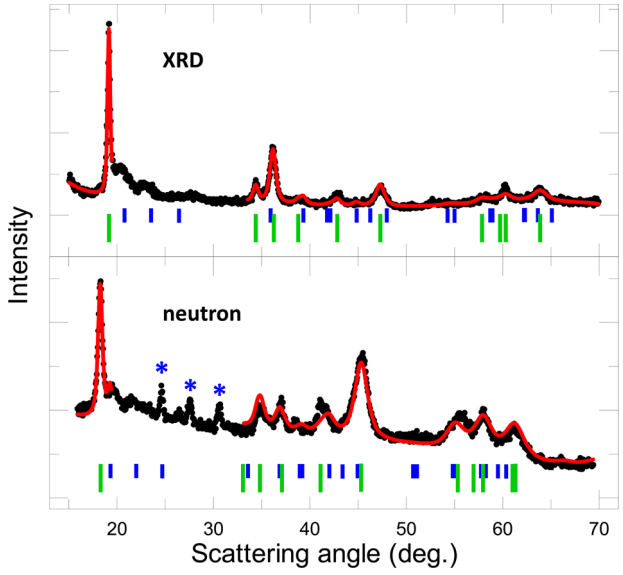

Figure 10. Fits of XRD (Cu Kα) and neutron (λ = 1.494 Å) scattering data for the chemically delithiated sample. Both fits were performed using two phases, both in the $R\bar{3}m$ space group, as discussed in the text. The green lines show the peak position of the major phase, phase 1, while the blue lines show the oxygen deficient minority phase, phase 2. The blue stars represent trace amounts of NO_2BF_4.

Table 5. Structural Parameters Obtained for Refining the XRD and Neutron Scattering Patterns for a Chemically Delithiated Sample[a]

phase	a (±0.01 Å)	c (±0.03 Å)	n_o (±0.1)	z_o (±0.01)	phase (%)
XRD					
Phase 1	3.07	13.96	1	0.40	86(3)
Phase 2	4.59	13.03	0.72	0.29	14(3)
Neutron					
Phase 1	3.08	14.11	1	0.40	83(3)
Phase 2	4.71	13.36	0.88	0.32	17(3)

[a]Two phases were used, both refined in the $R\bar{3}m$ space group. n_o is the occupation of the oxygen site (full occupation is 1) and z_o is the z coordinate of the oxygen site.

DOI: 10.1021/jacs.5b01424
J. Am. Chem. Soc. 2015, 137, 4804−4814

this refinement. There is excellent agreement for the more prominent phase (phase 1) for the parameters obtained from the neutron and XRD fits, and these show full oxygen occupancy. In contrast, phase 2 shows greater differences between the two fits, but this is attributed to the fact that there is only about 15% of this phase present such that its parameters are far less well constrained. Nonetheless, for both refinements phase 2 shows oxygen vacancies, such that we propose that the structure is made up of phase 1 in the bulk of particles and phase 2 at the surface of particles with oxygen deficiencies. Furthermore, the superstructure peaks were not refined for the chemically delithiated sample due to the large amount of computing required to fit patterns with stacking faults with one phase let alone two. Nonetheless, it is interesting to notice that peaks from phase 2 overlap with the superstructure peaks of phase 1, which accounts for the extra intensity of the superstructure peaks seen when fit with a single phase in Figure S.7. Figure S.8 shows the two structures. The oxygen lattice in phase 2 is considerably distorted, which is accommodated by a large increase in the *a* lattice parameter. Although it is impossible to state with certitude that this is the structure based on the current data, it is consistent with all data collected here. It is clear that refining the XRD and neutron data requires multiple phases (perhaps a distribution is the correct model) and that a distortion in the oxygen lattice in at least one of the phases is required to refine the neutron data adequately.

Discharge Capacity Below 3.0 V. As already discussed, the discharge plateau at about 4.0 V involves iron reduction and partial reduction of oxygenated species. However, when discharged to 2.0 V there is significant capacity below 3.0 V. All electrochemical data presented here show that discharging to 2.0 V results in a more rapid fade in the discharge plateau at 4.0 V with continued cycling. It is therefore important to understand the mechanism involved at these low potentials. Much of the low voltage capacity takes place below 2.6 V, as seen in Figure 1, in the voltage range where the alkyl carbonates react with superoxo species, as discussed in the introduction. Figure 2 shows that when cycled up to 4.4 V, even though there is no measurable oxygen release, there is release of carbon dioxide on subsequent charges (marked with blue arrows). This is consistent with the decomposition of reaction products which formed on the previous discharge. Alkyl carbonates in the electrolyte are therefore reacting directly on the surface of the particles or in solution, and then products attach to the surface of the particles.

Figure S.8 shows that the chemically delithiated sample has a discharge curve with this same plateau below 3.0 V (about 0.8 mol lithium can be reinserted, similar to that obtained when cycling to 4.4 V). In this case, there is no oxygen dissolved in the electrolyte as the cell was made with fresh electrolyte, so the carbonate electrolytes must be reacting directly at the surface of the material, presumably with the O_2^{n-} oxygenated species. To estimate how much capacity could come from oxygen dissolved in the electrolyte, we estimated the saturation point of oxygen gas in LP30 (1 M $LiPF_6$ in EC:DMC (1:1)) to be 0.073 mL O_2/mL electrolyte, i.e., the value for 1 M $LiPF_6$ in PC:DMC (1:1) from ref 25 and thus is an overestimate as EC has a lower Bunsen coefficient than PC. Assuming a four-electron transfer per O_2 unit, the maximum capacity originating from oxygen gas dissolved in electrolyte is therefore 10 mAh/g (for a typical electrode of 10 mg) or $\Delta x = 0.11$. This value assumes all oxygen from the electrolyte reacting by way of a four-electron process such that it is an overestimate, and yet this is still well below the typical capacity seen here (0.3−0.6 lithium on first discharge). Since no oxygen gas was detected by DEMS up to 4.4 V, we conclude that the electrolyte was not saturated with oxygen, and so the majority of the capacity seen around 2.6 V in fact comes primarily from electrolyte reacting directly with oxygenated species on the surface of the particles. Furthermore, Figure S.8b shows that a cell charged to 4.4 V, assembled into a new cell with fresh electrolyte and discharged continues to show the low voltage with 0.3 Li being inserted below 3.0 V identical to that seen in Figure 1a. This is again consistent with electrolyte reacting at the surface of particles at low potential, such that oxygen gas in the electrolyte is not required. The mechanisms proposed for the reaction of alkyl carbonates with superoxide in Li-air cells[9] can apply to reactions with oxygenated species on the surface of particles as well. We therefore propose that this mechanism is taking place at low potentials here. This also raises questions about the mobility of oxygenated species, where the greater importance of this reaction here, rather than in other lithium-rich oxides, may imply that the oxygenated species may migrate more easily to the surface of particles. However, for the present study it is sufficient to observe that the existence of this reaction confirms that some oxygenated species are not reduced above 3.0 V.

By contrast, for the sample charged to 5.0 V in Figure 1 there is both oxygen gas in the electrolyte (the electrolyte must be saturated for a significant amount of oxygen gas to be measured with DEMS) and oxygenated species on the surface of the particles, and the resulting capacity below 3.0 V is considerably larger (about 1.8 Li). This conclusion is confirmed by comparing the discharge curves of the two samples charged to 5.0 V: the sample in the DEMS cell where the gas is removed during cycling only has about 0.3−0.4 Li reinserted below 3.0 V, while the cell in the usual closed Swagelok cell had 1.8 Li. Thus, we can conclude that when charged to 4.2 V, alkyl carbonates react with oxygenated species on the next discharge primarily on the surface of the particles, while for charging up to 5.0 V both reactions on the surface of particles and in the electrolyte become possible on subsequent discharge, with the reaction in the electrolyte being more significant given that there is an excess of oxygen gas in the cell which was easily detected with DEMS. Nonetheless, regardless of where the reaction initiates, the surface of the electrodes becomes contaminated upon continued cycling, as observed in lithium-air battery research,[9−11] resulting in rapid capacity fade. One of the results of charging along the 4.2 V plateau is therefore to form a surface that is prone to the reaction with alkyl carbonates in the electrolyte which upon decomposition on the following charge contaminates the surface thereby accelerating the fade in the discharge plateau at 4.0 V. In order to more carefully determine these reaction mechanisms, considerable surface studies are required with a combination of XPS and FTIR measurements. For this study, seeing as this is a positive electrode material, it is sufficient to show that potentials below 3.0 V vs Li/Li+ should be avoided, as most if not all capacity in this range results from oxygenated species reacting with the carbonate-based solvents in the electrolyte.

■ DISCUSSION

The main elements of the voltage curve are now understood and summarized in Figure 11. Upon charge, iron and oxygen are both oxidized on the 4.2 V plateau. Subsequent discharge to 3.0 V reduces the iron and some of the oxygenated species. Any remaining oxygenated species on the surface of the particles are then prone to react with the electrolyte below 2.6 V. Subsequent cycling results in less and less of the iron being oxidized during

DOI: 10.1021/jacs.5b01424
J. Am. Chem. Soc. 2015, 137, 4804−4814

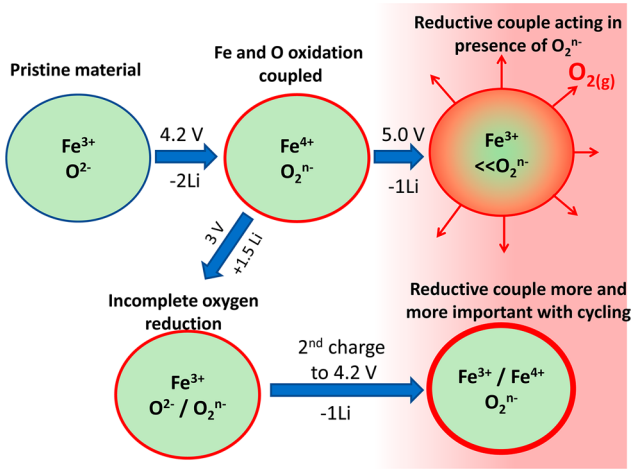

Figure 11. Schematic of the mechanisms involved during electrochemical cycling of Li_4FeSbO_6. Each circle represents a typical particle with the red outline being used to indicate that the surface is prone to electrolyte reaction at low voltage below 3.0 V. Of particular importance is the reductive couple acting on iron when sufficient oxygenated species are present in the sample.

charge, as the remaining O_2^{n-} results in reductive coupling if enough is present (this is seen in the in situ Mössbauer data in Table 2). In the case of charging to 5.0 V, this reductive couple is seen on first charge as there is a far greater amount of oxygenated species present.

A number of these features are new to our understanding of lithium-rich oxides. First, the metal and oxygen oxidation occurring simultaneously has not been seen in other systems, and it is best viewed as a two-electron removal from an FeO_6 octahedra. The fact that upon subsequent discharge the oxygen does not entirely reduce back to 2− is also new and demonstrates limited reversibility of the oxygen redox. It has been impossible to demonstrate this in other lithium-rich oxides since in such materials there is always a metal that can be reduced to below its pristine oxidation state during discharge such as Mn. Here, during first charge, 2.3 Li are removed up to 4.6 V (Figure 1a), which is assigned to being 1 electron from the Fe 3+ → 4+ transition and 1.3 electrons from O_2^{n-} species formation. Upon discharge, all iron is reduced at 3.0 V, but only 1.7 Li has been reinserted (or 1.5 in the in situ experiment). This therefore demonstrated that peroxo species do not cycle entirely reversibly; in fact only about 50−70% reversibility is seen. However, the first cycle involves many processes such as the formation of SEI, so it is important to verify that this irreversibility continues with cycling. Figure S.1 (right panel) shows that this observation is repeated with continued cycling, where a 15−20% irreversible capacity is seen consistently down to 3.0 V from cycles 2 to 9 in a cell cycled with the charge capacity limited to $\Delta x = 1.0$. This suggests that roughly 30% of the oxygenated species are not reduced during discharge upon continued cycling (it is critical to note here that over these cycles the voltage does not exceed 4.25 V so electrolyte oxidation is very limited, ref 26). For this material, irreversibility of the oxygenated species therefore results in capacity fade when the material is cycled between 3.0 and 4.4 V. Potential impacts of this process on other Li-rich materials are discussed in the final section of the Supporting Information.

The schematic diagram in Figure 11 also illustrates how oxygen is removed from the surface upon charging to 5.0 V, but that this is accompanied by the formation of more O_2^{n-} and a reductive couple acting on the iron such that it is reduced to 3+. Thus, comparing the pristine to the 5.0 V sample, all capacity comes from the oxygen (some due to oxygen release, but this is not nearly enough to account for the three Li removed so there is a lot of oxygenated species in the sample also). This reductive couple has also recently been demonstrated in Li−Ru−Sn−O materials using EPR.[27] Here, Li−Fe−Sb−O is therefore a second case where it has been conclusively shown that this process reduces the metal completely back to its initial oxidation state (this time it is Mössbauer data that corroborates the EPR findings in the Ru−Sn samples). This implies that all capacity in the fully charged state comes from oxygen oxidation and that metal oxidation is simply an intermediate step. It now becomes of critical importance to better understand what factors affect the reversibility of the O_2^{n-} species in the various systems already studied to then extrapolate to new systems that will provide less voltage fade. This will involve the design of new materials where the reduction taking place instead of the reduction of O_2^{n-} is more favorable to stable electrochemical performance.

CONCLUSIONS

The electrochemistry of Li_4FeSbO_6 proved to be very complex. On charge, both iron and oxygen oxidations occur simultaneously at 4.2 V, and oxygen release occurs at higher voltages. Upon discharge, the iron is reduced back to the pristine 3+ state with some reduction of oxygen, but this plateau at 4.0 V gradually decreases in length with cycling and coincides with a growth in capacity below 3.0 V. Li-rich oxides have been studied extensively, and participation of oxygen in the redox has been long speculated about in a number of layered oxide materials.[28] This particular material adds the following aspects to our understanding of these promising positive electrode materials:

(1) Oxygenated species O_2^{n-} can form simultaneously with metal oxidation in a multiple electron process. In NMC and Ru-based materials these two processes have always been distinct.

(2) The formation of oxygenated species is not entirely reversible (no efforts were made here to determine which species is irreversible, but as much as 30% of the capacity coming from oxygenated species seems to be irreversible during continued cycling here). This leads to irreversible capacity when cycled down to 3.0 V in the Li−Fe−Sb−O material since none of the metals can be reduced below their initial oxidation state (Fe^{3+} and Sb^{5+}) in this voltage range. By contrast, in NMC materials, such irreversibility would lead to activation of manganese which can be reduced around 3.3 V, and this redox peak grows with time to give the voltage fade studied extensively. Similarly, in Li−Ru−Ti−O materials, titanium is reduced below its initial 4+ state during every discharge cycle.[5]

(3) At high voltage, the metals are reduced to their initial oxidation states as oxygen gas and a large amount of oxygenated species are produced. Such a reductive couple has been seen before, but only with EPR for Ru-based compounds has it ever been conclusively shown that it is sufficient to return the metals to their pristine oxidation states. This shows that all the capacity at the maximally charged states in this material (and perhaps other Li-rich oxides as well) is stored solely in the oxygen. It is also interesting to note that no such reductive couple has been found to be active in NMC materials (though small changes in Ni and Co K-edge XANES features during the

DOI: 10.1021/jacs.5b01424
J. Am. Chem. Soc. 2015, 137, 4804−4814

high voltage plateau are reported).[8] Further consideration of this process is required in such compositions spaces.

(4) The resulting shearing from structural changes due to the intermediate state (where both Fe and O are oxidized) combined with the effects of removing oxygen from the surface of particles is very destructive to the material, with both XRD and Mössbauer showing that this is more violent than chemical delithiation.

Thus, the peculiar electrochemistry of this lithium-rich material has proved valuable in advancing our understanding of oxygen redox in lithium-ion batteries.

■ ASSOCIATED CONTENT

Supporting Information

Experimental details, supporting data referred to throughout the main text, citations for refs 29, 30, 31 and a discussion regarding how this work impacts our understanding of Li-rich Ni−Mn−Co oxide materials. This material is available free of charge via the Internet at http://pubs.acs.org".

■ AUTHOR INFORMATION

Corresponding Author

*jean-marie.tarascon@college-de-france.fr

Notes

The authors declare no competing financial interest.

■ ACKNOWLEDGMENTS

E.M. thanks the Fonds de recherche du Québec − Nature et Technologies and Alistore − European Research Institute for funding this work as well as the European community I3 networks for funding the neutron scattering research trip. The authors also thank RS2E for funding this research, V. Pomjakushin for his help in performing the neutron experiments, B. Budic for performing the ICP-OES measurements as well as A. Mahmoud and R.P. Hermann who performed the ^{121}Sb Mössbauer measurements.

■ REFERENCES

(1) Koga, H.; Croguennec, L.; Ménétrier, M.; Douhil, K.; Belin, S.; Bourgeois, L.; Suard, E.; Weill, F.; Delmas, C. *J. Electrochem. Soc.* **2013**, *160*, A786.

(2) Lu, Z.; Beaulieu, L. Y.; Donaberger, R. A.; Thomas, C. L.; Dahn, J. R. *J. Electrochem. Soc.* **2002**, *149*, A778.

(3) Thackeray, M. M.; Johnson, C. S.; Vaughey, J. T.; Hackney, S. A. *J. Mater. Chem.* **2004**, *15*, 2257.

(4) Sathiya, M.; Rousse, G.; Ramesha, K.; Laisa, C. P.; Vezin, H.; Sougrati, M. T.; Doublet, M.-L.; Foix, D.; Gonbeau, D.; Walker, W.; Prakash, A. S.; Ben Hassine, M.; Dupont, L.; Tarascon, J.-M. *Nat. Mater.* **2013**, *12*, 827.

(5) Sathiya, M.; Abakumov, A. M.; Foix, D.; Rousse, G.; Ramesha, K.; Saubanère, M.; Doublet, M. L.; Vezin, H.; Laisa, C. P.; Prakash, A. S.; Gonbeau, D.; Van Tendeloo, G.; Tarascon, J.-M. *Nat. Mater.* **2014**, *14*, 230.

(6) Yu, S.-H.; Yoon, T.; Mun, J.; Park, S.; Kang, Y.-S.; Park, J.-H.; Oh, S. M.; Sung, Y.-E. *J. Mater. Chem. A* **2013**, *1*, 2833.

(7) Gu, M.; Belharouak, I.; Zheng, J.; Wu, H.; Xiao, J.; Genc, A.; Amine, K.; Thevuthasan, S.; Baer, D. R.; Zhang, J.-G.; Browning, N. D.; Liu, J.; Wang, C. *ACS Nano* **2013**, *7*, 760.

(8) Koga, H.; Croguennec, L.; Ménétrier, M.; Mannessiez, P.; Weill, F.; Delmas, C.; Belin, S. *J. Phys. Chem. C* **2014**, *118*, 5700.

(9) Freunberger, S. A.; Chen, Y.; Peng, Z.; Griffin, J. M.; Hardwick, L. J.; Bardé, F.; Novák, P.; Bruce, P. G. *J. Am. Chem. Soc.* **2011**, *133*, 8040.

(10) Mizuno, F.; Nakanishi, S.; Kotani, Y.; Yokoishi, S.; Iba, H. *Electrochemistry* **2010**, *78*, 403.

(11) Xu, W.; Viswanathan, V. V.; Wang, D.; Towne, S. A.; Xiao, J.; Nie, Z.; Hu, D.; Zhang, J.-G. *J. Power Sources* **2011**, *196*, 3894.

(12) Yabuuchi, N.; Yoshii, K.; Myung, S.-T.; Nakai, I.; Komaba, S. *J. Am. Chem. Soc.* **2011**, *133*, 4404.

(13) McCalla, E.; Abakumov, A.; Rousse, G.; Reynaud, M.; Sougrati, M. T.; Budic, B.; Mahdoux, A.; Dominko, R.; Van Tendeloo, G.; Hermann, R. P.; Tarascon, J.-M. *Chem. Mater.* **2015**, *27*, 1699.

(14) Zvereva, E. A.; Savelieva, O. A.; Titov, Y. D.; Evstigneeva, M. A.; Nalbandyan, V. B.; Kao, C. N.; Lin, J.-Y.; Presniakov, I. A.; Sobolev, A. V.; Ibragimov, S. A.; Abdel-Hafiez, M.; Krupskaya, Y.; Jähne, C.; Tan, G.; Klingeler, R.; Büchner, B.; Vasiliev, A. N. *Dalton Trans.* **2013**, *42*, 1550.

(15) McCalla, E.; Rowe, A. W.; Camardese, J.; Dahn, J. R. *Chem. Mater.* **2013**, *25*, 2716.

(16) Menil, F. *J. Phys. Chem. Solids* **1985**, *46*, 763.

(17) Dedushenko, S. K.; Perfiliev, Y. D.; Tcheboukov, D. E.; Pankratov, D. A.; Kiselev, Y. M. *Mendeleev Commun.* **1999**, *9*, 211.

(18) Demazeau, G.; Buffat, B.; Ménil, F.; Fournès, L.; Pouchard, M.; Dance, J. M.; Fabritchnyi, P.; Hagenmuller, P. *Mater. Res. Bull.* **1981**, *16*, 1465.

(19) Nishijima, M.; Takeda, Y.; Imanishi, N.; Yamamoto, O.; Takano, M. *J. Solid State Chem.* **1994**, *113*, 205.

(20) Laha, S.; Natarajan, S.; Gopalakrishnan, J.; Morán, E.; Sáez-Puche, R.; Alario-Franco, M.-A.; Dos Santos-García, A. J.; Pérez-Flores, J. C.; Kuhn, A.; García-Alvarado, F. *Phys. Chem. Chem. Phys.* **2015**, *17*, 3749.

(21) Sathiya, M.; Ramesha, K.; Rousse, G.; Foix, D.; Gonbeau, D.; Prakash, A. S.; Doublet, M.-L.; Hemalatha, K.; Tarascon, J.-M. *Chem. Mater.* **2013**, *25*, 1121.

(22) Lippens, P. E. *Solid State Commun.* **2000**, *113*, 399.

(23) Koga, H.; Croguennec, L.; Ménétrier, M.; Mannessiez, P.; Weill, F.; Delmas, C. *J. Power Sources* **2013**, *236*, 250.

(24) Fell, C. R.; Qian, D.; Carroll, K. J.; Chi, M.; Jones, J. L.; Meng, Y. S. *Chem. Mater.* **2013**, *25*, 1621.

(25) Read, J.; Mutolo, K.; Ervin, M.; Behl, W.; Wolfenstine, J.; Driedger, A.; Foster, D. *J. Electrochem. Soc.* **2003**, *150*, A1351.

(26) Wang, D. Y.; Xia, J.; Ma, L.; Nelson, K. J.; Harlow, J. B.; Xiong, D.; Downie, L. E.; Petibon, R.; Burns, J. C.; Xiao, A.; Lamanna, W. M.; Dahn, J. R. *J. Electrochem. Soc.* **2014**, *161*, A1818.

(27) Sathiya, M.; Ramesha, K.; Rousse, G.; Foix, D.; Gonbeau, D.; Guruprakash, K.; Prakash, A. S.; Doublet, M.-L.; Tarascon, J.-M. *Chem. Commun.* **2013**, *49*, 11376.

(28) Tarascon, J. M.; Vaughan, G.; Chabre, Y.; Seguin, L.; Anne, M.; Strobel, P.; Amatucci, G. *J. Solid State Chem.* **1999**, *147*, 410.

(29) FAULTS program is distributed within the FullProf Suite, available at http://www.ill.eu/sites/fullprof/index.html, accessed April 1, 2015.

(30) Jumas, J.-C.; Stievano, L.; Sougrati, M. T.; Fullenwarth, J.; Fraisse, B.; Leriche, J.-B. *Analyse des caracteristiques d'un matériau d'électrode d'une cellule électrochimique*. Patent WO 2014033402 A1, August 28, 2013.

(31) Berg, E. J.; Novák, P. *ECL Annual Report 2012*, Paul Scherrer Institut: Villigen PSI, Switzerland, pp 47; http://www.psi.ch/lec/AnnualReportsUebersichtsTabelle/ECL-Annual-Report_2012.pdf.

DOI: 10.1021/jacs.5b01424
J. Am. Chem. Soc. 2015, 137, 4804−4814